Behavioral/Cognitive

Evidence for Abstract Codes in Parietal Cortex Guiding Prospective Working Memory

Jongmin Lee,[1] David De Vito,[1] Jacob A. Miller,[2] and Derek Evan Nee[1]
[1]Department of Psychology, Florida State University, Tallahassee, Florida 32304 and [2]Department of Psychology, University of Miami, Coral Gables, Florida 33124

The recent past helps us predict and prepare for the near future. Such preparation relies on working memory (WM) which actively maintains and manipulates information providing a temporal bridge. Numerous studies have shown that recently presented visual stimuli can be decoded from fMRI signals in visual cortex (VC) and the intraparietal sulcus (IPS), suggesting that these areas sustain the recent past. Yet, in many cases, concrete, sensory signals of past information must be transformed into the abstract codes to guide future cognition. However, this process remains poorly understood. Here, human participants of either sex used WM to maintain a separate spatial location in each hemifield wherein locations were embedded in a learned spatial sequence. On each trial, participants made a sequence-match decision to a probe and then updated their WM with the probe. The same abstract sequence guided judgments in each hemifield, allowing the separate detection of concrete spatial locations (hemifield-specific) and abstract sequence positions (hemifield-general) and also tracking of representations of the past (last location/position) and future (next location/position). Consistent with previous reports, concrete past locations held in WM could be decoded from VC and IPS. Moreover, in anticipation of the probe, representations shifted from past to future locations in both areas. Critically, we observed abstract coding of future sequence positions in the IPS whose magnitude related to speeded performance. These data suggest that the IPS sustains abstract codes to facilitate future preparation and reveal a transformation of the sensory past into abstract codes guiding future behavior.

Key words: abstraction; fMRI; parietal cortex; prospective; visual cortex; working memory

Significance Statement

To act efficiently, we must use the recent past to prepare for what comes next. For this purpose, working memory (WM) is critical. Although substantial research has shown that WM retains recently presented sensory information, preparation for the future involves abstraction wherein shared meaning is aggregated while superfluous sensory details are discarded. The mechanisms underlying this process remain unclear. Analyzing functional MRI signals in the intraparietal sulcus (IPS), we found that distinct sensory states with shared predictive meaning were initially maintained in a sensory-like fashion but over time, became aggregated indicative of abstraction. Abstraction was associated with behavioral efficiency highlighting its role in preparation. These findings reveal neural mechanisms supporting the transformation from past to future in WM.

Introduction

Working memory (WM) refers to the maintenance and manipulation of information no longer available to the senses (Baddeley, 1992; Curtis and D'Esposito, 2003; D'Esposito and Postle, 2015; Nee and D'Esposito, 2018). WM is central to higher-level cognition as many of our behaviors require extending the recent sensory past to prepare for the near future (Fuster, 1990, 2001; Rainer et al., 1999; Nobre and Stokes, 2019). Despite its importance for future-oriented cognition, most WM studies focus on how the recent past is maintained. Numerous studies have revealed that visual sensory codes can be decoded from fMRI activation patterns in occipital and parietal cortices (Harrison and Tong, 2009; Serences et al., 2009; Christophel et al., 2012, 2015; Albers et al., 2013; Sprague and Serences, 2013; Sprague et al., 2014, 2016; Ester et al., 2015; Bettencourt and Xu, 2016; Lorenc et al., 2018; Rademaker et al., 2019; Li and Curtis, 2023). Such findings have given rise to the sensory recruitment hypothesis which states that WM is supported by the

Received Sept. 6, 2025; revised Nov. 11, 2025; accepted Dec. 15, 2025.
Author contributions: D.D.V. and D.E.N. designed research; D.D.V. performed research; J.L. and D.D.V. analyzed data; J.L., J.A.M., and D.E.N. edited the paper; J.L. and D.E.N. wrote the paper.
We thank Michael Dicalogero for help with collecting the data. This work was supported by Startup Funds from Florida State University (D.E.N.).
The authors declare no competing financial interests.
Correspondence should be addressed to Jongmin Lee at jongmin.lee.529@gmail.com.
This paper contains supplemental material available at: https://doi.org/10.1523/JNEUROSCI.1719-25.2025
https://doi.org/10.1523/JNEUROSCI.1719-25.2025

sustained maintenance of sensory information in those same sensory cortices involved in initial perception (Pasternak and Greenlee, 2005; Serences, 2016; Scimeca et al., 2018; Sreenivasan and D'Esposito, 2019).

However, when preparing for the future, we are often guided by nonsensory codes. Consider finding a friend in a grocery store who has a common shopping routine (e.g., produce then bread then deli counter). If upon arriving at the store, they text you that they are getting produce, you might head toward the bread aisle in anticipation of where they will be by the time you walk over. This example illustrates that prospective actions are often guided by abstract codes. Abstraction is a process by which shared features are aggregated (Ho et al., 2019; Courellis et al., 2024), facilitating generalization and knowledge transfer across contexts (Badre et al., 2010; Collins and Frank, 2013; Badre, 2024). For example, knowledge of your friends' shopping routine (abstract code) may also help you find them in a different grocery store (new context). Despite the importance of abstraction, there is a critical gap in our understanding of the abstract representations that reside in-between sensation and action which prospectively and flexibly guide cognition.

Abstract coding increases with synaptic distance from primary cortices (Mesulam, 1998; Brincat et al., 2018). For visuo-spatial processing, the intraparietal sulcus (IPS) is downstream of visual cortical areas of the occipital cortex (e.g., V1–V4; VC). Although visual WM is often decoded similarly in VC and IPS (Christophel et al., 2012; Sprague and Serences, 2013; Sprague et al., 2014, 2016), some evidence suggests that IPS WM representations are more robust to distraction (Bettencourt and Xu, 2016; Lorenc et al., 2018; Rademaker et al., 2019). Abstraction is thought to result in a distractor-resistant, stable, low-dimensional coding format (Murray et al., 2017; Rademaker et al., 2019). Hence, we reasoned that abstract codes that facilitate prospection would be relatively more prominent in the IPS than VC.

This study used fMRI to investigate the mechanisms underlying using the recent past to prepare for the future. Human participants performed a sequence-matching task which probed whether a presented spatial location followed the last spatial location in a predefined sequence (Fig. 1). The sequence (Fig. 1*a*) was abstract in that it generalized to spatial locations in either hemifield. Moreover, employing a sequence afforded using the recent past (most recently presented location) to prepare for the near future (next location in the sequence). Through this task, we examined concrete (spatial location), abstract (sequence position), retrospective (previous location/position), and prospective (next location/position) coding in visual and parietal cortices. We predicted that both IPS and VC would show initial evidence of concrete, retrospective coding consistent with past works. However, we anticipated the emergence of abstract and prospective coding in the IPS consistent with a top-down code to guide future expectations. This result would provide evidence for abstract codes guiding prospective WM.

Materials and Methods

Participants. Twenty-two participants were recruited from the Tallahassee area for this experiment. All participants underwent an initial screening process to ensure that they understood and could adequately perform the task. Informed consent was obtained according to the guidelines set forth by the Office for Human Subjects Protection and Florida State University Institutional Review Board. For the experiment, a total of three scanning sessions were planned. Two participants were unable to tolerate the scanner environment, and one participant was lost due to a scheduling conflict. An additional four participants were removed from the study following the first scanning session due to insufficient data quality (e.g., two for poor task accuracy, two for excessive head motion). These data were excluded from further analyses. The remaining 15 participants (age range, 18–23; mean age, 20.1; 10 female) were analyzed for this report. One participant did not complete the last scanning session due to a technical issue with the remaining participants completing all three sessions.

fMRI experimental design. In the fMRI scanner, participants performed a sequence working memory task. In the task, participants were required to maintain two spatial locations, one in each visual hemifield, each of which were drawn from a five-location sequence tracing a star (Fig. 1). These stimuli were used as references for the probes. On each trial, a cue was presented at the center of the screen for 500 ms, pointing to either the left or right visual hemifield, indicating that an upcoming probe would appear in that respective visual hemifield (task-relevant visual hemifield). For all but the first cue, cues were preceded (pre-cue delay) and followed (post-cue delay) by 7500 ms of fixation. After the post-cue delay, a probe was presented in the task-relevant visual hemifield for 500 ms. Participants were asked to determine whether the spatial location of the currently presented probe sequentially followed the reference (i.e., the spatial location of the last stimulus presented in the same visual hemifield). The spatial location of the probe then was used as the reference for the next probe in the same visual hemifield. Thus, the reference in the probed hemifield was updated in each trial.

Half of the probes followed the reference in the sequence, thereby requiring a "match" response. "Non-match" probes were pseudorandomly and equally drawn from the three spatial locations remaining after excluding the sequence "match" and the reference (i.e., there were no stimulus repeats). Trials were equally distributed to cue the left and right visual hemifields and to require even numbers of switches and repeats of the visual hemifield of the preceding trial. Each run began with the presentation of two location stimuli for 1,500 ms which served as the initial reference locations. A delay of 2,500 ms separated the initial stimuli from the first cue. During the experiment, participants were asked to fixate their gaze on a fixation cross at the center of the screen and not move their eyes. Adherence to these instructions was monitored by eye tracking. Fourteen out of 15 participants completed three scanning sessions, while one participant completed only two scanning sessions due to a technical issue. Each scanning session was carried out on separate days. Each scanning session consisted of four experimental runs and 50 trials per experimental run. There was a short break between experimental runs.

Stimuli and apparatus. The experiment was programmed with E-Prime software version 2.0 (Psychology Software Tools). The probe stimulus was a blue circle with a diameter of ~2°. Stimuli were presented between 5.5 and 15.25° of visual angle left and right and between 3.32 and 4.68° of visual angle above and below a central fixation point.

MRI acquisition. MRI data were collected on a Siemens 3T Prisma with a 32-channel head coil. The participant observed visual stimuli in the scanner using a mirror attached to the head coil, which reflected the visual stimuli onto a projection screen. Responses were recorded using a four-button MR-compatible button box (Current Designs), with participants using the index finger of each hand to input their responses.

Functional imaging data were obtained using an EPI sequence provided by the Center for Magnetic Resonance Research (CMRR) at the University of Minnesota: voxel dimensions of $2 \times 2 \times 2$ mm; TR, 2,000 ms; TE, 33.8 ms; flip angle, 45°; FOV, 192 mm^2; multiband factor, 4. Prior to each functional scan, four dummy scans were conducted to ensure image stabilization. Phase and magnitude images at the same resolution of the functional images were acquired to assess and correct for magnetic field inhomogeneity. Additionally, a high-resolution T1-weighted MPRAGE image was collected for spatial normalization ($384 \times 384 \times 256$ matrix of 0.667 mm3 isotropic voxels; TR, 1,840 ms; echo time, 2.9 ms; flip angle, 9°).

MRI data preprocessing. Preprocessing on image data was done in SPM12 (https://www.fil.ion.ucl.ac.uk/spm/) unless otherwise specified. DICOM format was converted into NIfTI format. The origin of all

images in each participant was manually adjusted to the anterior commissure. Functional image data underwent spike correction to mitigate the influence of artifacts using AFNI's 3dDespike routine (http://afni.nimh.nih.gov/afni), as well as slice timing correction for each run, head motion correction via a six-parameter rigid body transformation, and unwarping and correction of motion-by-susceptibility distortions using the FieldMap toolbox (Andersson et al., 2001). Based on the realignment parameters, linear, squared, differential, and squared differential movement parameters were calculated (24 in total; Lund et al., 2005). These parameters were regressed out of the functional images, and the resultant residuals were high-pass filtered at 1/128 Hz. These data were used for all described analyses.

Structural image data were coregistered to the functional image data. Then, segmentation was performed on structural image data to acquire gray and white matter probability maps (Ashburner and Friston, 1997) from which spatial normalization warping to and from the MNI template was calculated.

ROI selection. We selected the left and right intraparietal cortex (IPS) along with the left and right visual cortex (VC) as the regions of interest (ROIs) given their role in maintaining working memory (Harrison and Tong, 2009; Serences et al., 2009; Ester et al., 2015; Bettencourt and Xu, 2016; Lorenc et al., 2018; Rademaker et al., 2019). ROI masks were created using a probabilistic atlas (Wang et al., 2015) with a 90% probability threshold. VC ROIs were created by combining V1v, V1d, V2v, V2d, V3v, V3d, and hV4. IPS ROIs were created by combining IPS0-5. These ROIs were warped to native space for each individual.

Multivariate fMRI analyses. The BrainIAK toolbox implemented in Python was used to conduct decoding analyses (Kumar et al., 2020). All decoding analyses were performed on preprocessed BOLD responses from the ROIs of each participant. To appropriately balance factors for classification, consecutive pairs of runs were concatenated. The concatenated BOLD data of each ROI were temporally z-scored to ensure that voxel activities were scaled to the same range. Only correct trials were analyzed. After removing error trials, we equalized the number of trials of each spatial location in each run to match the smallest count among them by randomly sampling the larger number of trials of each spatial location resulting in ∼8 trials per concatenated run per location on average. Such random sampling and cross-validation were repeated 1,000 times.

To train and test a classifier (L2-regularized, multinomial logistic regression), we implemented a leave-one-pair-out cross-validation procedure. The decoding outputs of each participant were calculated as the average decoding outputs across all iterations. During each cross-validation iteration, we applied univariate feature selection using an ANOVA (f-classif function in the scikit-learn Python library; Pedregosa, 2011) with a threshold alpha level of 0.05 on the training data. The features selected based on the training data were used on the testing data. Since this procedure resulted in a variable number of features as a function of ROI and time point, we repeated the analyses using a fixed number of features (300, which approximated the lower bound of the number of features selected by the above procedure) which produced the same patterns of results as reported in the main text (Fig. S6) indicating that the results are robust to the specifics of feature selection. The L2 penalty was the value of 1, which was used to train the classifier. For the decoding analysis, we excluded the initial trial of each run as the timing and visual presentation of this trial differed from the others.

Multivariate fMRI analyses: temporal generalization decoding analysis. Temporal generalization decoding analysis (King and Dehaene, 2014) was conducted to assess transformations of representations over time. Classifiers were trained to classify 10 distinct categories representing the spatial locations of stimuli (five locations in each hemifield) based on the average fMRI activation patterns over the last two time points of the post-cue delay period (12 and 14 s post-stimulus onset). Since we anticipated that participants would form expectations of to-be-probed location, the classifier was trained using the labels of the location corresponding to a match probe. Then, the trained classifier was tested to classify each TR of the independent testing data (8 TRs in total; from 0 to 14 s from the onset of the probe). The temporal generalization decoding analysis produced classifier evidence corresponding to each of the 10 spatial locations at each time point. We specifically tracked evidence for the retrospective-relevant ("Retro-rel"), retrospective-irrelevant ("Retro-irrel"), prospective-relevant ("Pro-rel"), and prospective-irrelevant ("Pro-irrel") locations (Figs. 1*c*, 2*a*). During the pre-cue delay, the classifier evidence for the just-probed spatial location was categorized as "Retro-rel," and the last probed spatial location in the uncued hemifield was categorized as "Retro-irrel." During the post-cue delay of the repeat condition, the classifier evidence for the next spatial locations of "Retro-rel" and "Retro-irrel" in the sequence were categorized as "Pro-rel" and "Pro-irrel," respectively. In the switch condition, the classifier evidence corresponding to the next spatial locations of "Retro-irrel" and "Retro-rel" in the sequence were categorized as "Pro-rel" and "Pro-irrel," respectively. For each time point, classifier evidence for each of the four categories of interest were averaged across trials for each subject and submitted to statistical analysis.

Prior work has suggested that representations during WM and perception are distinguishable (Rademaker et al., 2019; Lorenc et al., 2020; Chunharas et al., 2025). Hence, the analyses above focused on training the very end of the post-cue delay to maximize separation from sensory signals and hone in on mnemonic codes (Iamshchinina et al., 2021; see also Riggall and Postle, 2012; Myers et al., 2015; Rademaker et al., 2019). For completeness, we repeated the procedures above using the last two time points of the pre-cue delay (4 and 6 s post-stimulus onset) to train classifiers. This timing corresponds to the peak of hemodynamic signals following a stimulus allowing the ability to determine the extent to which the results reflecting more sensory-like signals show the same patterns. In this case, the classifier was trained using the labels of the just-probed location. These data are reported in Figure S4*a*. We note that due to the circular nature of the sequence, the classifier training labels are somewhat arbitrary. That is, we could alternatively have used prospective training labels during the pre-cue delay as we did with the late delay above (i.e., assuming that expectations for the next location in the sequence dominate the signals during the pre-cue delay). In this case, we would not expect further transitions through the sequence (e.g., if the training label is R1, we would not expect to see evidence for R2 at any point during the trial). However, during testing, we observed diminished classifier evidence of the training-matching labels and increased classifier evidence of labels matching the next location in the sequence, thus validating our assumptions and procedure (Fig. S4*a*).

Training and testing were performed separately for each of the four ROIs (left and right IPS and VC). Given similarity in the results in each hemifield, left and right hemifields were averaged together to summarize a given brain area (e.g., left and right IPS results were averaged to characterize the IPS).

Multivariate fMRI analyses: cross-visual hemifield decoding analysis. Cross-visual hemifield decoding analysis was performed by training a classifier on the five sequence positions presented on the one visual hemifield [e.g., the left (right) visual hemifield] and testing the classifier on the five sequence positions presented on the other visual hemifield [e.g., the right (left) visual hemifield]. Decoding was conducted in a time-resolved manner, involving training and testing the classifier within the same TR. The label at each TR during the pre-cue delay was based on the just-probed stimulus, while the label at each TR during the post-cue delay was based on the last probed stimulus in the cued hemifield. Notably, since each TR was trained and tested independently from other TRs, this analysis is agnostic to whether the same position is being decoded across TRs or whether a systematic shift (e.g., from the last probed position to the next position in the sequence) occurs at some point and when. Because of this, whether the position is labeled as the just/last probed position (retrospective) or the next position in the sequence (prospective) is arbitrary.

Representational similarity analysis. We conducted a representational similarity analysis (RSA; Kriegeskorte et al., 2008) on the preprocessed BOLD data to examine the transformation of the neural

representation of WM across time points. To setup the data for RSA, consecutive pairs of runs were concatenated in the same way as in the decoding analyses. Then, data were split into training and testing sets by using a leave-one-pair-out-cross-validation procedure. For each iteration of the cross-validation, univariate feature selection was performed using an ANOVA with a threshold alpha level of 0.05 on the training data (note similar patterns of results were obtained by fixing the number of features at 300; Fig. S6). The selected features (voxels) were then z-scored as a collection, followed by z-scoring within each feature. Based on these normalized features on the training data, we selected samples corresponding to the 10 spatial locations at the last two time points of the post-cue delay (12 and 14 s post-stimulus onset). Then, we calculated the average value of the selected samples for each spatial location to form the training representations (10 spatial locations). For the testing data, we used the same features selected on the training data and applied z-score normalization in the same manner as was done for the training data. Then, we selected samples corresponding to the 10 spatial locations for each time point. For each time point, we averaged the patterns of activation for each of the 10 spatial locations, respectively, to form the testing representations. Then, for each time point, we calculated the correlation coefficient among the 10 training representations and the 10 testing representations. In other words, eight RSA matrices were formed, one per time point, showing the representational similarity between the 10 spatial locations of the training set and the 10 spatial locations in the testing set. Each RSA matrix was submitted to model-based regression analysis (see below) for each iteration of the cross-validation.

As we did for the temporal generalization decoding above, we repeated these procedures using pre-cue delay (4 and 6 s) trained data for completeness (Fig. S4*b*,*c*).

Representational similarity analysis: model-based regression. We performed multiple linear regression (Eq. 1), using the vectorized correlation coefficient RSA matrices described above as the dependent variable (r) and a set of vectorized model RSA matrices as regressors. This analysis estimated the unique contribution of each model RSA matrix to the correlation coefficient RSA matrix. Below describes five model RSA matrices with details:

1. A matrix representing hemifield spatial attention ('SA") reflecting similarity among stimuli presented on the same visual hemifield, but dissimilarity among stimuli presented on the opposite visual hemifields. Similarity was assigned a regressor value of 1 and dissimilarity was assigned a regressor value of −1. This model captures broad spatial attention directed to the task-relevant visual hemifield.
2. A matrix representing the spatial location of the reference ("Concrete Retro"). Here, distance-dependent similarity was accounted for by computing the distance in visual angle among locations in the same hemifield. The distance in visual angle between two locations was scaled by the maximum distance among any two locations such that a location with itself received a value of 1 and the maximally distant two locations received a value of −1. Between hemifield locations were assigned a value of 0 as these dissimilarities are already captured by the SA regressor. Note that since we assume that training patterns reflect the prospective location, retrospective regressors are shifted back one location in the sequence (e.g., a trained pattern of L2 would be expected to appear as L1 early in the trial).
3. A matrix representing the location following the reference in the sequence ("Concrete Pro"). In this case, since we assume that training patterns reflect the prospective location, this matrix resembles the identity matrix along with distance-dependent similarity as above.
4. A matrix representing the abstract sequence position for the reference stimulus ("Abstract Retro"), wherein the values of the second model RSA matrix ("Concrete Retro") were flipped in the horizontal direction. By doing so, we modeled cross-hemifield generalizability of the abstract sequence position of the past. Note that the ideal matrix corresponding to a retrospective abstract sequence position would be the summation of the "Concrete Retro" and "Abstract Retro" matrices as described. However, such a matrix would induce collinearity with the "Concrete Retro" matrix. Hence, the "Abstract Retro" matrix as described captures additional variance attributed to cross-hemifield generalization over-and-above within-hemifield distance-dependent similarity.
5. A matrix representing the abstract sequence position for the next location in the sequence ("Abstract Pro"), wherein the values of the third model RSA matrix ("Concrete Pro") were flipped in the horizontal direction. By doing so, we modeled the cross-hemifield generalizability of the abstract sequence position of the upcoming future. As with the "Abstract Retro" matrix, this matrix captures additional variance attributed to cross-hemifield generalization over-and-above within-hemifield distance-dependent similarity.

$$r \sim \beta_0 + \beta_1 \mathrm{SA} + \beta_2 \mathrm{Concrete\ Retro} + \beta_3 \mathrm{Concrete\ Pro} + \beta_4 \mathrm{Abstract\ Retro} + \beta_5 \mathrm{Abstract\ Pro}. \quad (1)$$

For each iteration of the cross-validation procedure, we estimated beta weights for each time point using the equation (Eq. 1). The beta weights obtained from the model-based regression across the iterations were averaged for each participant.

Multidimensional scaling analysis. To visualize the representational geometry of WM, we performed multidimensional scaling (MDS). For each subject, ROI, TR, and location, we trained and tested a classifier to decode each of the 10 spatial locations. Training was performed in two different manners. First, the classifier was trained and tested on a TR-by-TR basis as we did with the cross-hemifield decoding analyses. This allows examination of the dominant geometry over time. Second, the classifier was trained on the last two time points of the post-cue delay (12 and 14 s) and was tested at each time point, as we did with the temporal generalization decoding analyses. This allows emphasis on mnemonic codes. In each case (dominant geometry decoding, mnemonic code decoding), when testing each of the 10 spatial locations, classifier evidence was obtained for each of the 10 trained spatial locations and averaged across the time points of the pre-cue and post-cue delays, respectively. This resulted in 10 (testing locations) × 10 (training locations) matrices indicating the confusability of each spatial location for each delay period. Then for each delay period, each of the 15 participants' matrices were vertically concatenated resulting in 150 (testing locations × participants) × 10 (training locations) pre- and post-cue matrices, respectively. These group-level classifier evidence matrices were then used to calculate 10 × 10 correlation distance matrices. These correlation distance matrices were submitted to MDS using the cmdscale function implemented in R. The first three dimensions accounting for 70.7–96.5% variance (Fig. S5*a*,*d*) were visualized. Each location was projected onto a three-dimensional space showing the WM representational spaces of the ROIs by time (Fig. 6*b*,*c*).

To statistically quantify the WM representational geometry, we repeated the same procedures separately at the individual participant level. Then, for each participant, we calculated the Euclidean distances among the 10 spatial locations based on the three-dimensional coordinates of the spatial locations, resulting in a Euclidean distance matrix (top row in Fig. S5*g*,*h*). Since we supposed that the WM representational geometry might reflect either retinotopic or sequence position space, we estimated a matrix representing each space, using the visual angle distance of spatial locations (bottom row in Fig. S5*g*,*h*). That is, the retinotopic matrix (left column of bottom row in Fig. S5*g*) was created based on the visual angle distance among the 10 spatial locations. The sequence position matrix (right column of bottom row in Fig. S5*g*) assumed that locations corresponding to the same sequence position were identical and thus corresponded to the visual angle distance between five spatial locations with zero distance between distinct spatial locations with the same sequence positions. In order to measure the similarity between the Euclidean distance and visual angle distance matrices, we calculated the Pearson's correlation between the vectorized upper triangle portion of the Euclidean distance and visual angle distance matrices (excluding the diagonal) and performed Fisher's Z transformation for the statistical quantification.

Statistical analysis. Statistical tests for decoding analyses were based on permutation testing with 1,000 iterations. Permutation testing avoids issues that can occur when testing against theoretical chance distributions at small sample sizes (Combrisson and Jerbi, 2015). For each iteration, the classifier was trained and tested with shuffled decoding labels, resulting in 15 null decoding accuracies (1 per participant) for each time point (0, 2, 4, 6, 8, 10, 12, and 14 s) and each ROI (left/right IPS and VC). These null decoding accuracies were submitted to a one-tailed one-sample *t* test against chance (one-tailed since decoding accuracy is not expected to be significantly below chance) and two-way repeated-measures ANOVAs, resulting in null *T* or null *F* values, which formed null distributions (Figs. 2, 3). Note that for *t* tests, this procedure is identical to comparing actual decoding accuracy to a null distribution of decoding accuracies but generalizes more easily to repeated-measures ANOVAs. *p* values were the percentage of values in the null distribution that were greater than or equal to the observed *T* or *F* values obtained from the intact data, resulting in 0.001 as the lower limit for the *p* value. We applied this calculation to other permutation statistical tests. (Note that for two-tailed tests, *p* values were calculated based on the null distribution of the absolute null *T* value and the absolute observed value). Similar to the above, statistical tests on beta weights obtained from RSA shown in Figure 5 were based on permutation testing over 1,000 iterations. For each iteration, the shuffled correlation coefficient RSA matrix was submitted to model-based regression:

$$\begin{aligned}\text{shuffled } r \sim\ & \beta_0 + \beta_1 \text{SA} + \beta_2 \text{Concrete Retro} \\ & + \beta_3 \text{Concrete Pro} + \beta_4 \text{Abstract Retro} \\ & + \beta_5 \text{Abstract Pro.}\end{aligned} \quad (2)$$

For each iteration, we obtained 15 null beta weights (1 per subject) for each time point, each ROI, and each regressor (Concrete Retro, Concrete Pro, Abstract Retro, and Abstract Pro). These null beta weights were submitted to one-tailed one-sample *t* tests against a value of 0 (one-tailed because only beta weights above a value of 0 are expected), two-tailed paired *t* tests and a two-way RM ANOVA, resulting in null *T* or null *F* values, which formed the null distributions (Fig. 5*a*,*b*).

The statistical test on the brain–behavior correlation analysis was based on a permutation test with 1,000 iterations. For each iteration, we shuffled the participant order of 15 observed averaged beta weights of interest and correlated it with the intact participant order of behavioral data, resulting in the null distribution of the null *T* values (Fig. 5*c*).

Statistical test on MDS shown in Figure 6 was based on permutation testing with 1,000 iterations. Since the output of the cmdscale function in R was used as the coordinates corresponding to WM representations for 10 spatial locations in 3D space, we shuffled the outputs but kept the label of 10 spatial locations intact for each iteration. Using the shuffled multidimensional 3D coordinates, we calculated the null Euclidean distances between 10 spatial locations, generating a null Euclidean distance matrix. These matrices were then correlated with either the intact retinotopic matrices or sequence position matrices by vectorizing the upper triangular portion of each matrix. For the statistical test, the correlation value was Fisher's *Z* transformed, resulting in 15 null Fisher's *Z* values (1 per subject) for each time point, each ROI, and each space (retinotopic and position). These null Fisher's *Z* values were submitted to two-tailed paired *t* tests, and two-way/three-way RM ANOVAs, resulting in the null distribution of the null *T* and *F* values (Fig. 6*d*,*e*).

For all statistical tests across multiple time points, multiple comparisons were corrected using false discovery rate (FDR; Benjamini and Hochberg, 1995).

Data and code availability. Preprocessed data and all original code have been deposited at Open Science Framework and are publicly available at https://osf.io/n5ake/ as of the date of publication.

Results

Despite the importance of abstraction to WM and cognition, few studies have examined abstract coding in support of WM. Some evidence has demonstrated that concrete sensory information of the past can be recoded into a more abstract format such as translating a motion cloud to a line (Kwak and Curtis, 2022; Duan and Curtis, 2024). Moreover, some studies have demonstrated that when forthcoming actions can be anticipated, prospective action codes are maintained (van Ede et al., 2019; Boettcher et al., 2021; Henderson et al., 2022; Nasrawi and van Ede, 2022; Shushruth et al., 2022). However, we know little about the abstract representations that reside in-between sensation and action which prospectively and flexibly guide WM for the future. To fill this gap, we designed a paradigm in which WM was guided by an abstract sequence wherein we define abstraction as the ability to generalize over contexts or instances (Badre and D'Esposito, 2007; Nee and D'Esposito, 2016; Bernardi et al., 2020; Badre et al., 2021; Kwak and Curtis, 2022; Courellis et al., 2024; Duan and Curtis, 2024). Here, each visual hemifield formed a distinct context containing spatial locations that needed to be tracked independently via WM. Critically, spatial locations in each visual hemifield transitioned according to a common sequence (Fig. 1*a*) such that the sequence formed an abstract code guiding WM.

Participants separately and continuously tracked spatial locations in the left and right visual hemifields (Fig. 1*b*). On each trial, a cue indicated the relevant hemifield for the forthcoming probe affording a prospective prediction of the sequencing-matching location. Participants indicated whether the spatial location of the probe followed the spatial location of the last stimulus in the cued hemifield (reference). Half of the probes were matches while half were non-matches with non-match probes equally drawn from the three non-matching spatial locations excluding the reference (i.e., there were no stimulus repeats). After responding, the spatial location of the probe became the reference for the next probe of the same hemifield. The cue was separated from the previous (pre-cue delay) and forthcoming (post-cue delay) probes allowing for periods to track WM codes of different forms (retrospective vs prospective, concrete/location vs abstract/position; Fig. 1*c*).

Behavioral data indicated that participants performed the task well (mean accuracy = 94.8%). To verify that participants appropriately prioritized relevant information (i.e., the cued hemifield), we separately characterized trials in which the cue indicated the same visual hemifield as the previous trial ("Repeat") or the opposite visual hemifield ('Switch"). As anticipated, reaction times (RT) and error rates (ER) were larger in "Switch" (610.1 ms, 7.4%) relative to "Repeat" trials (594.5 ms, 3.1%; $t_{(14)} = 2.53$, $p = 0.024$ for reaction time; $t_{(14)} = 3.44$, $p = 0.004$ for error rate, paired *t* tests; Fig. 1*d*) consistent with a cost for switching priority. These data confirm that participants performed the task as expected.

Location codes are transformed over time

We hypothesized that WM codes would transform over time trading off from retrospective to prospective (Fig. 1*c*). Some work suggests that sensory and mnemonic signals are multiplexed in the visual cortex and IPS (Rademaker et al., 2019; Chunharas et al., 2025). Past work indicates that classifiers trained on the late delay period data can isolate mnemonic signals (Iamshchinina et al., 2021; see also Riggall and Postle, 2012; Myers et al., 2015; Rademaker et al., 2019). In order to focus on mnemonic representations, classifiers were trained on patterns drawn from the end of the post-cue delay (12 and 14 s post-stimulus onset) and then tested across time points from 0 to 14 s (see Fig. S4*a* for classifiers trained at the end of the pre-cue delay). Classifiers were trained and tested separately for each region-of-interest (ROI; left and right IPS and VC) to

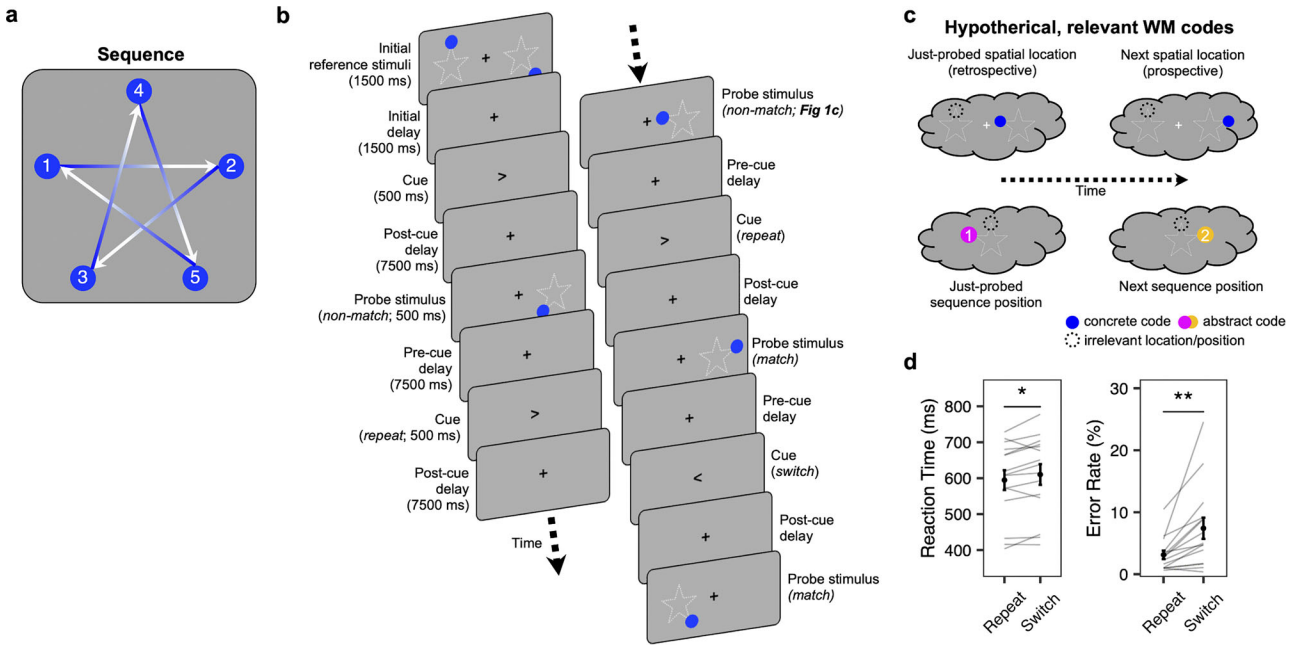

Figure 1. Procedures and behavioral performance. ***a***, The sequence consisted of five points forming a star. Arrows indicate the sequence ordering such that position 2 followed position 1, position 3 followed position 2, etc. Position 5 transitioned back to position 1 such that the sequence was circular. ***b***, Task procedure. Each trial consisted of a pre-cue delay, a cue, and a post-cue delay. At the start of each run, initial spatial locations were presented in the left and right visual hemifields. After an initial delay, a cue indicated the task-relevant visual hemifield wherein a forthcoming probe would be presented following a post-cue delay. Participants determined whether the spatial location of the probe followed the spatial location of the last item that appeared in the same hemifield. Half of the probes were sequence matches (e.g., position 2 following position 1) while half were non-matches (e.g., position 3 following position 1). The dotted lines indicating the star trace are used for illustrative purposes and did not appear in the actual task. ***c***, The potential transformation of relevant WM codes over time. After the probe stimulus presentation, the spatial location of the just-probed stimulus (blue; concrete, retrospective code; hemifield-specific) and its sequence position (pink; abstract, retrospective code; hemifield-general) could be maintained in WM. To optimally prepare for the future, these hypothetical codes would be transformed over time to the next location(blue)/position(orange). Irrelevant (uncued) representations are included for completeness (dashed lines) but are not a main focus here. ***d***, Mean reaction time and error rates. Behavioral performance was better when the cue indicated the same visual hemifield as the previous trial ("Repeat") relative to when the cue indicated the other visual hemifield ('Switch"). Each line on the bar graph represents each participant. Bold dots indicate the mean across participants with error bars representing ±1 standard error of mean. $*p < 0.05$, $**p < 0.01$.

discriminate the activation patterns corresponding to each of the 10 spatial locations.

If WM codes transform over time, the location held in mind at the end of the post-cue delay just prior to the probe (i.e., prospective) would differ from the location encoded during and shortly after stimulus presentation (i.e., retrospective). Therefore, we labeled each training pattern as though it coded for the cued, prospective location (Fig. 2*a*). Then we tested the classifier separately for each time point. We separately detailed classifier evidence for the retrospective spatial location in the relevant hemifield (retrospective-relevant; "Retro-rel"), the retrospective spatial location in the irrelevant hemifield (retrospective-irrelevant; "Retro-irrel"), the prospective spatial location in the relevant hemifield (prospective-relevant; "Pro-rel"), and the prospective spatial location in the irrelevant hemifield (prospective-irrelevant; "Pro-irrel"; Fig. 1*c*). Relevance refers to the just-probed hemifield in the pre-cue period and the cued hemifield in the post-cue period. The results were averaged across hemispheres for each of the IPS and VC, respectively.

Figure 2 depicts the classifier evidence for the retrospective-relevant ("Retro-rel") and prospective-relevant ("Pro-rel") locations. In both the IPS and VC, classifier evidence for the retrospective-relevant spatial location was significantly above-chance levels during the pre-cue delay, whereas it dropped to chance during the post-cue delay [note, all statistical tests are performed against a permutation null (Combrisson and Jerbi, 2015); see Materials and Methods]. In contrast, classifier evidence for the prospective-relevant spatial location showed the opposite pattern (Fig. 2*b*). Separating the data by post sequence-match (Fig. S1*a*) and post sequence-non-match (Fig. S1*b*) and by repeat (Fig. S1*c*) and switch (Fig. S1*d*) trials revealed that these patterns were shaped, but not driven by carry-over from prior trials (sequence-match/non-match) or periods (repeat/switch). To further quantify these patterns, we averaged each classifier evidence within each delay period (from 2 to 6 s, "pre-cue"; from 10 to 14 s, "post-cue") and submitted the data to a 2 (period: "pre-cue" vs "post-cue") × 2 (location: "Retro-rel" vs "Pro-rel") repeated-measures ANOVA for each of the IPS and VC (Fig. 2*c*). We observed a significant interaction of period and location in both the IPS ($F_{(1,14)} = 19.35$, $p < 0.001$) and VC ($F_{(1,14)} = 16.33$, $p < 0.01$) confirming a shift from retrospective to prospective coding in each area.

To examine whether the timing of these transitions differed by region, we performed ROI × location repeated-measures ANOVA at individual time points. Significant interactions were observed at 2, 4, and 6 s ($F_{(1,14)} > 4.9$, $ps < 0.01$). Follow-up paired t tests revealed that the VC showed stronger evidence for the retrospective relevant item than the IPS at 2 and 4 s ($ts_{(14)} > 3.31$, $ps < 0.01$), whereas the IPS showed stronger evidence for the prospective relevant item than the VC at 6 s ($t_{(14)} = 2.66$, $p = 0.019$). These data suggest that although both areas transition from coding retrospective to prospective items, the VC more strongly codes for retrospective locations during the early delay, while the IPS shifts toward coding for prospective locations earlier than the VC.

Most evidence for either the retrospective-irrelevant or prospective-irrelevant spatial locations were at or under chance (Fig. S2), indicating that decodable representations in the IPS and VC were restricted to prioritized items as consistent with

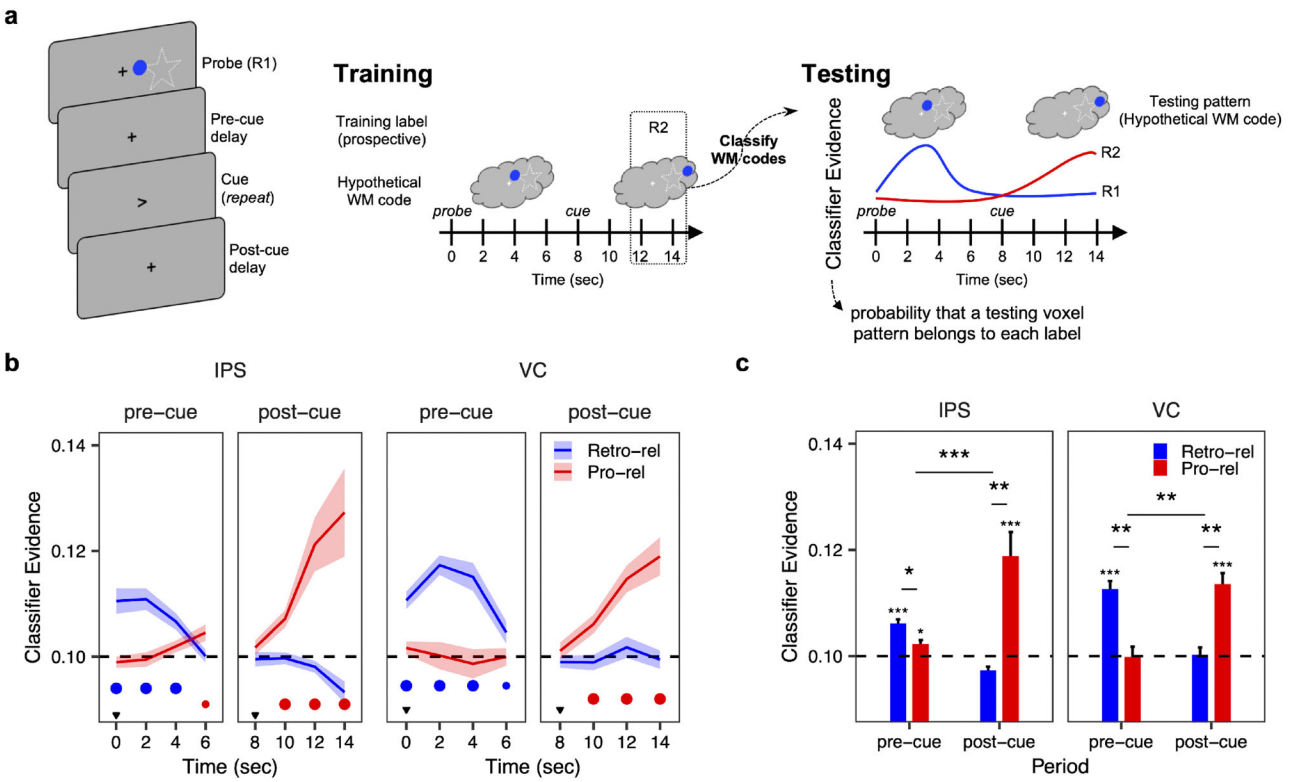

Figure 2. Tracking retrospective and prospective codes over time. ***a***, Decoding strategy to track retrospective and prospective WM codes over time. Classifiers were trained using data from the end of the post-cue delay (12 and 14 s) and then tested at each time point. ***b***, Retrospective-relevant ("Retro-rel") refers to the classifier evidence corresponding to the spatial location of the just-probed item. Prospective-relevant ("Pro-rel") refers to the classifier evidence corresponding to the next spatial location following the reference (location following the previous probe in the pre-cue delay; location following the previous probe of the cued hemifield in the post-cue delay). The significance at each time point is denoted by small and medium dots, representing $q < 0.05$ and $q < 0.01$, respectively (FDR corrected). The inverted triangles denote the time points of the presentation of the probe and the cue, respectively. ***c***, Average of classifier evidence in each delay period (from 2 to 6 s, "pre-cue" period; from 10 to 14 s, "post-cue" period) for each ROI. $*p < 0.05$, $**p < 0.01$, $***p < 0.001$. Error bars represent ±1 standard error of mean.

substantial past work (Lewis-Peacock et al., 2012; Sprague et al., 2016; LaRocque et al., 2017; Lorenc et al., 2020; Yu et al., 2020). In subsequent analyses, we will therefore focus on relevant items.

Taken together, the results indicate that WM was transformed over the delay periods from retrospectively representing the past to prospectively representing expectations for the future.

Abstract sequence information is coded in the IPS

In the current task, anticipation of prospective spatial locations in each visual hemifield was guided by the same abstract spatial sequence. Abstraction is commonly defined as generalization across contexts (Bernardi et al., 2020; Badre et al., 2021; Kwak and Curtis, 2022; Courellis et al., 2024; Duan and Curtis, 2024). Here, each visual hemifield formed a distinct context. To test for abstract coding of sequence, we examined the extent to which representations generalized across hemifields by training a classifier using representations from one hemifield and testing it with representations from the other hemifield (cross-visual hemifield decoding; Fig. 3*a*). Training and testing were performed separately for each TR using labels of the relevant sequence position. (Note that since training and testing is performed separately for each TR, this analysis is agnostic to whether the retrospective or prospective sequence position is being decoded.) We found significant cross-visual hemifield decoding during both the pre-cue and post-cue delays in the IPS with decoding accuracy ramping up over time during both phases (Fig. 3*b*). In contrast, in the VC, the classifier showed above-chance decoding accuracy only during a single time point in the pre-cue delay. To better quantify this result, we averaged the decoding accuracies from 2 to 6 s to form the "pre-cue" period and from 10 to 14 s to form the "post-cue" period separately for each region and submitted the data to a region (IPS, VC) × period ("pre-cue," "post-cue") repeated-measures ANOVA. Abstract sequence position was more strongly decoded in the IPS relative to the VC (main effect of region $F_{(1,14)} = 8.74$, $p = 0.008$; Fig. 3*c*). Neither the main effect of period nor the interaction between period and region was significant. Collectively, although there was some weak evidence for abstract codes in the VC, abstract sequence information was prominent across delay periods in the IPS.

Concrete and abstract codes of working memory are transformed over time

To better examine the extent to retrospective, prospective, concrete, and abstract codes are multiplexed versus tradeoff over time, we turned to representational similarity analysis (RSA; Kriegeskorte et al., 2008). For each of the 10 spatial locations, we extracted the patterns of activation in each of our four ROIs (left and right IPS and VC). Training patterns were formed by averaging over the last two time points of the post-cue delay as we did above (see Fig. S4*b* for training during the pre-cue delay). Then in a testing set, for each time point, we calculated the correlation similarity between the activity pattern at that time point and each training pattern (Fig. 4*a*). This was done separately for each ROI. We then decomposed representations in the IPS and VC into (1) coarse representations of the attended hemifield (spatial attention); (2) fine-grained representations of the retrospective, relevant spatial location (concrete retrospective); (3)

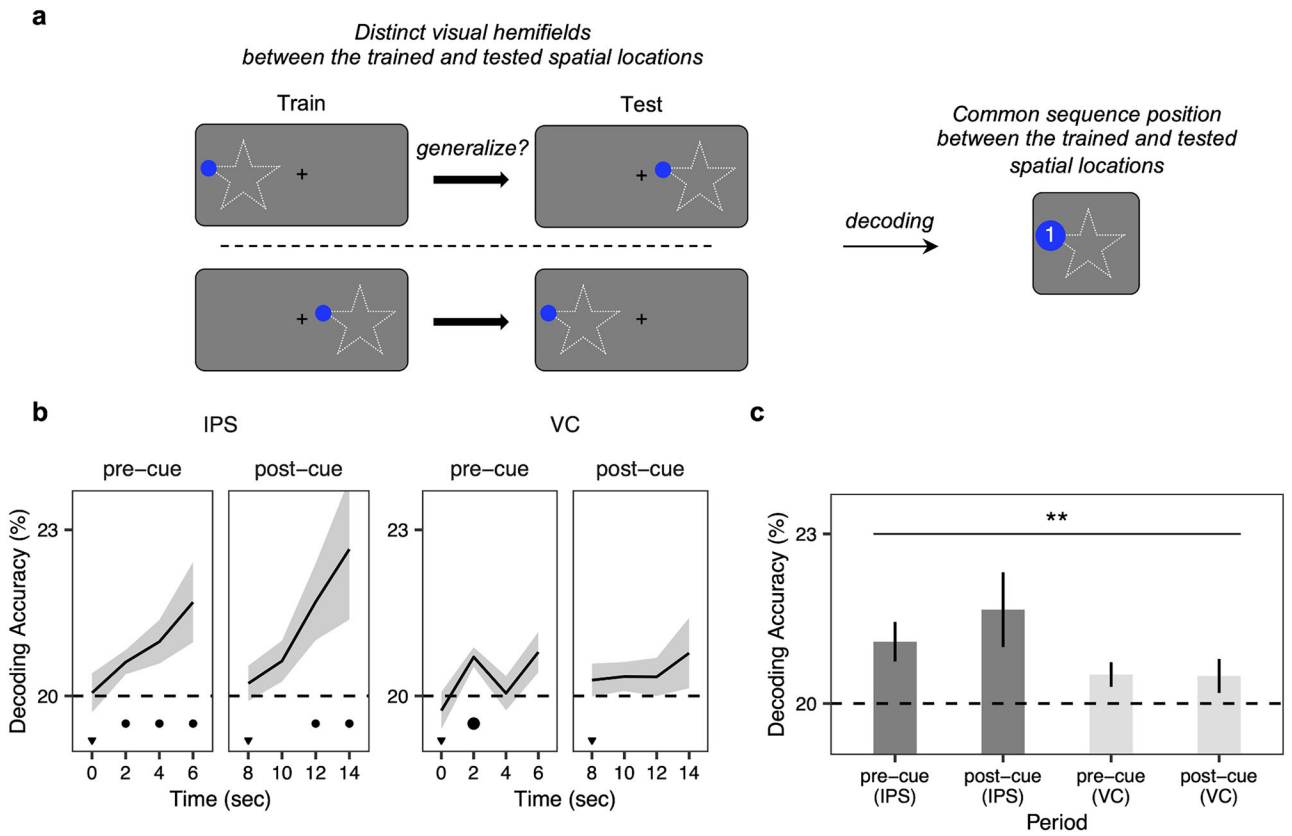

Figure 3. Decoding abstract sequence positions. ***a***, Schematic illustration of the cross-visual hemifield decoding analysis. Abstract coding was operationally defined based on generalization of decoding across visual hemifields. ***b***, The result of the cross-visual hemifield decoding analysis, in which training and testing the classifier were performed on different visual hemifields, respectively. The significance at each time point is denoted by small and medium dots, representing $q < 0.05$ and $q < 0.01$, respectively (FDR corrected). The shaded regions represent ±1 standard error of mean. The inverted triangles in black denote the time points of the presentation of the probe stimulus and the cue, respectively. ***c***, Average of decoding accuracies from "pre-cue" (2–6 s) and "post-cue" (10–14 s) period in each ROI. The horizontal dashed line indicates the chance level of 20%. $^{**}p < 0.01$. Error bars represent ±1 standard error of mean.

fine-grained representations of the prospective, relevant spatial location (concrete prospective); (4) abstract representations of the retrospective sequence position (abstract retrospective); and (5) abstract representations of the prospective sequence position (abstract prospective) using multiple linear regression (Lapate et al., 2022; Jones et al., 2024). Each regressor represents a representational similarity matrix corresponding to a hypothetical pure representation (see Materials and Methods; Fig. 4*a*). The regressors incorporated distance-dependent similarity based upon normalized visual angle (i.e., nearby locations are more similar to one another than far locations). Concrete regressors were formed by training/testing in the same hemifield, while abstract regressors were formed by training/testing across hemifields. Based on the analyses above, we expected that retrospective codes would transition to prospective codes, both concretely and abstractly (Fig. 4*b*).

As shown in Figure 5*a*, we found evidence consistent with these predictions. In both the IPS and VC, a concrete retrospective code emerged early during the pre-cue delay but diminished over time until it was absent by the end of the post-cue delay. The fall of concrete retrospective codes was mirrored by rising concrete prospective codes which started before the cue (van Ede et al., 2021) and peaked at the end of the post-cue delay. In the IPS, we observed a similar tradeoff in abstract codes from retrospective to prospective. However, abstract codes were not significantly observed in the VC. Interestingly, abstract and prospective codes emerged at the same time point in the IPS (4 s post-stimulus onset) and preceded the onset of concrete prospective codes in the VC (6 s post-stimulus onset). Although the sluggishness of the BOLD signal precludes detailed timing information, the data are consistent with the use of abstract sequence position to inform concrete expectations of the future. In other words, the stimulus spatial location (concrete retrospective) may be translated into an abstract sequence position (abstract retrospective) which can then be transformed into the next abstract sequence position (abstract prospective), affording a prediction of the probe spatial location (concrete prospective).

To further quantify these observations, for each region, we averaged the beta weights from 2 to 6 s to form the "pre-cue" period and directly contrasted the IPS and VC with paired *t* tests (Fig. 5*b*). Spatial attention was more strongly represented in the VC than IPS ($t_{(14)} = -3.85$, $p = 0.006$), whereas concrete retrospective coding did not differ between the regions ($t_{(14)} = 0.77$, $p = 0.46$). In contrast, the IPS showed stronger coding of the abstract retrospective ($t_{(14)} = 2.79$, $p = 0.013$), concrete prospective ($t_{(14)} = 3.05$, $p = 0.014$), and abstract prospective ($t_{(14)} = 2.81$, $p = 0.008$) codes in the pre-cue period. These data indicate that abstract and prospective codes emerge earlier in the IPS than VC. Next, for each region, we averaged the beta weights from 10 to 14 s to form the "post-cue" period. These data indicated that spatial attention remained stronger in the VC than IPS ($t_{(14)} = -3.88$, $p = 0.003$), whereas concrete ($t_{(14)} = 2.84$, $p = 0.013$) and abstract ($t_{(14)} = 2.59$, $p = 0.025$) prospective coding remained stronger in the IPS than the VC (Fig. 5*b*). Finally, we cross-correlated the magnitudes of

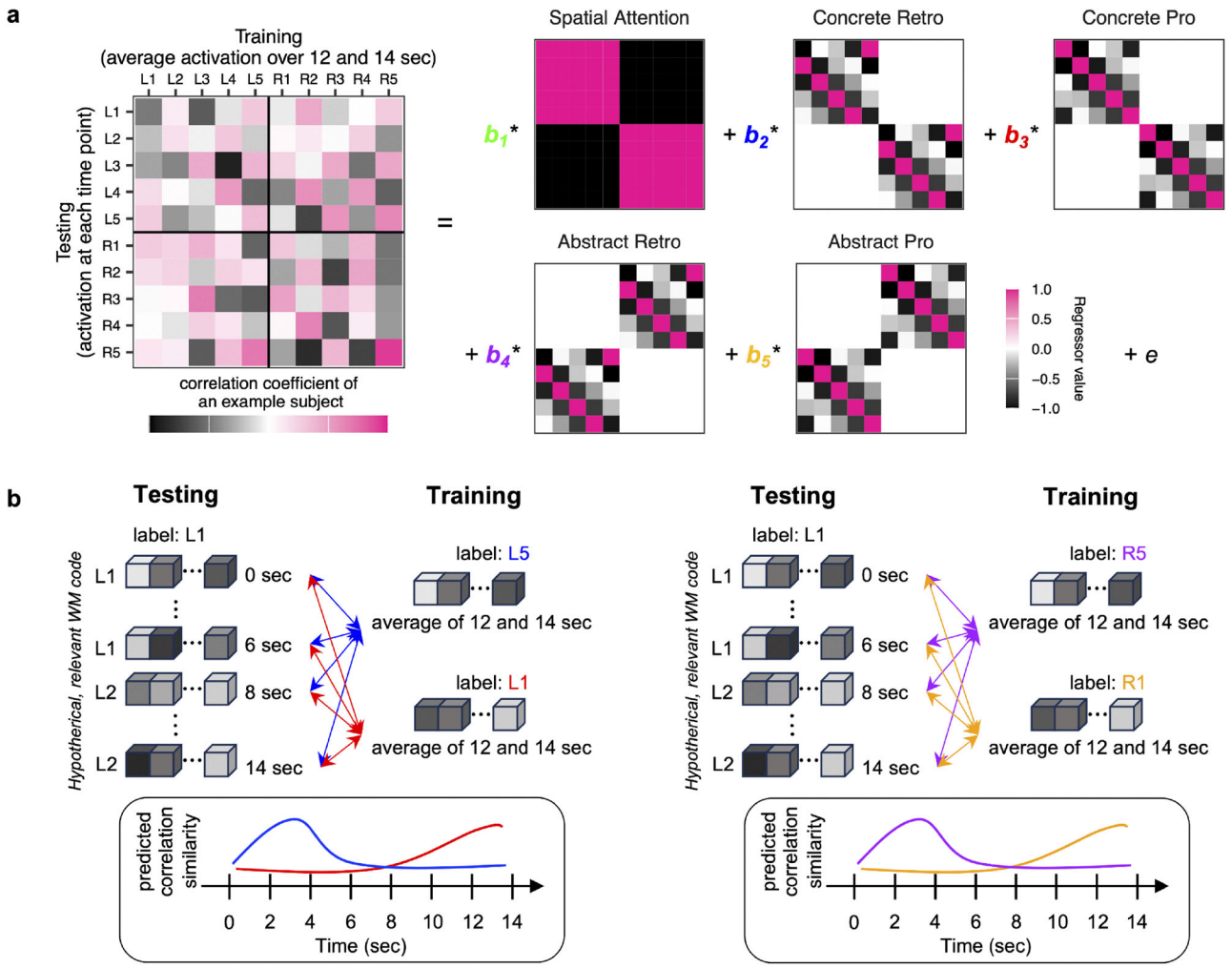

Figure 4. Schematic illustration of the representational similarity analysis. ***a***, The left depicts an example representational similarity matrix formed by correlating training patterns of each location with testing patterns of each location. These matrices were submitted to multiple linear regression using regressors denoting idealized matrices of spatial attention, concrete retrospective coding, concrete prospective coding, abstract retrospective coding, and abstract prospective coding. We estimated the beta weight for each regressor at each time point. Training patterns were formed by averaging the activation patterns at 12 and 14 s post-stimulus onset. Hypothetical models were created assuming that the training patterns reflect the prospective location/position. Hence, retrospective models reflect a correspondence between testing patterns (e.g., L1, the first row) that correspond to the location/position preceding the training pattern (e.g., L5) with increasing dissimilarity as a function of increasing retinotopic distance. ***b***, Schematic of the predicted correlation similarities representing a transition between concrete retrospective to concrete prospective coding (left) and abstract retrospective to abstract prospective coding (right). For example, the training pattern of L5 (or R5 if abstract coding) was assumed to have the highest similarity with the testing pattern of L1 during the "pre-cue" delay period. In contrast, the training pattern of L1 (or R1 if abstract coding) was assumed to have the highest similarity with the testing pattern of L1 during the "post-cue" delay period.

prospective codes during the post-cue period. Abstract prospective codes in the IPS were correlated with concrete prospective codes in the IPS ($r = 0.78$, $p = 0.002$), which were, in turn, correlated with concrete prospective codes in the VC ($r = 0.62$, $p = 0.016$). However, abstract prospective codes in the IPS were not themselves correlated with concrete prospective codes in the VC ($r = 0.21$, $p = 0.454$). Moreover, the relationship between concrete prospective codes in the IPS and VC remained after partialing out shared variance with abstract prospective codes in the IPS ($r = 0.62$, $p = 0.018$). Although low sample sizes render these findings preliminary, these data are consistent with a transformation and relay of codes supporting WM.

Next, we examined how representational codes were related to behavioral performance. We reasoned that behavioral preparedness (i.e., faster RTs) would be related to prospective coding, rather than retrospective coding. Consistent with this idea, RT was negatively related to abstract prospective coding during the post-cue period in the IPS ($r = -0.63$, $p = 0.014$), but not VC ($r = -0.33$, $p = 0.232$). A similar, nonsignificant trend was observed for concrete prospective coding in the IPS ($r = -0.42$, $p = 0.129$). However, this trend appeared to be driven by shared variance with abstract coding (described above) as partialing out concrete prospective coding left the relationship between abstract prospective coding in the IPS and RT largely intact ($r = -0.5264$, $p = 0.055$) while the reverse was not true ($r = 0.1029$, $p = 0.72$). Moreover, concrete prospective coding in the VC was unrelated to RT and reversed in sign ($r = 0.19$, $p = 0.508$). Similarly, concrete and abstract retrospective coding during the pre-cue period was non-significantly related to RT ($ps > 0.3$). These results were replicated when using inverse efficiency indicating that the results could not be attributed to a speed-accuracy tradeoff (Fig. S3). Although conclusions should be taken with some measure of caution due to the sample sizes, collectively, these data suggest that abstract prospective coding in the IPS facilitates future behavioral performance.

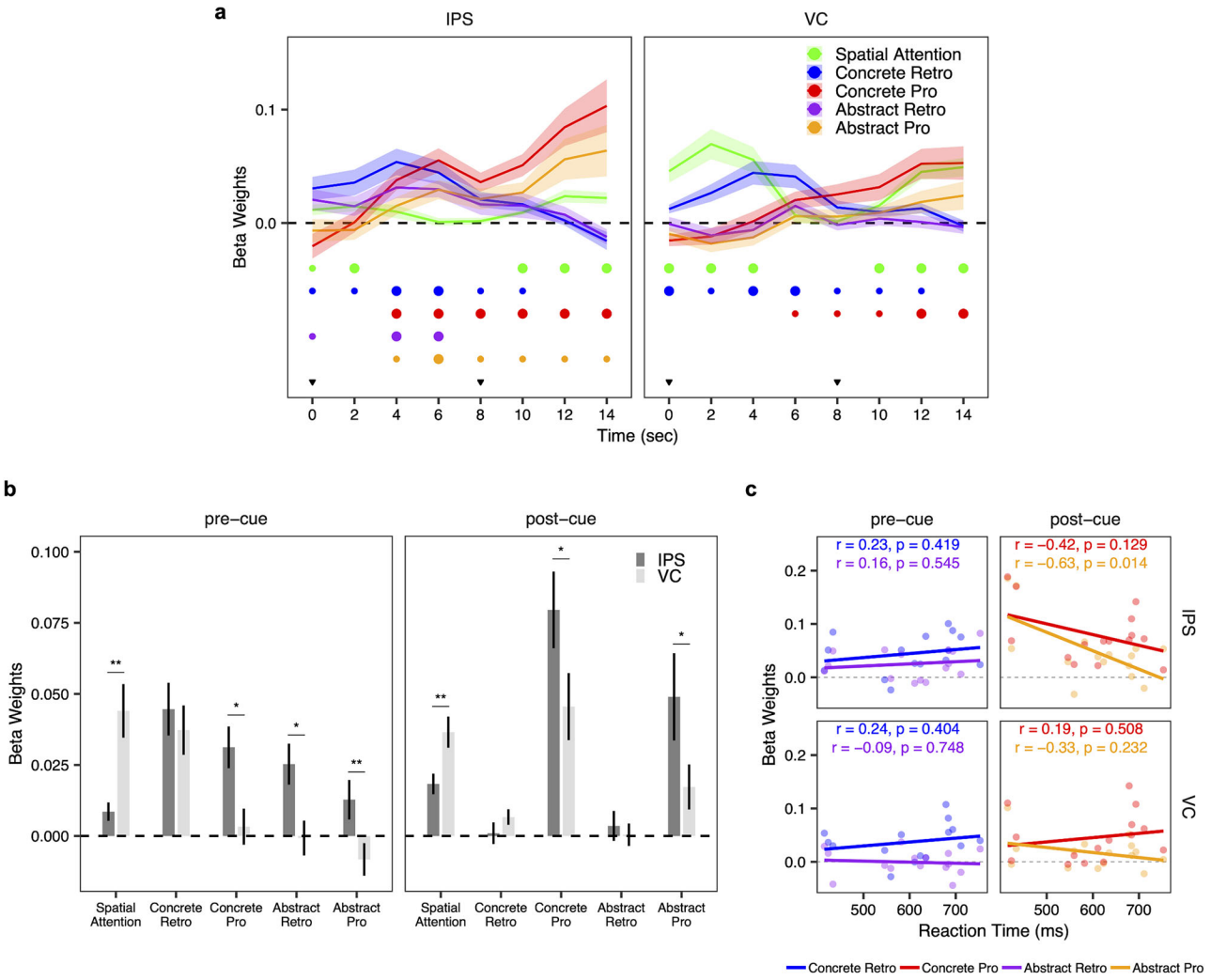

Figure 5. Simultaneous and dynamic coding of the past and future. ***a***, The estimated beta weights for each regressor at each time point. The beta weights were compared against a value of 0 and corrected for multiple comparisons using false discovery rate (FDR). The significance at each time point is denoted by small and medium dots, representing $q < 0.05$ and $q < 0.01$, respectively (FDR corrected). The shaded regions represent ±1 standard error of mean. The inverted triangles in black denote the time points of the presentation of the probe stimulus and the cue, respectively. ***b***, To contrast the IPS and VC, spatial attention and each WM code were separately formed by averaging beta weights during the "pre-cue" period (2–6 s) and the "post-cue" period (10–14 s) in each ROI. Error bars represent ±1 standard error of mean. *$p < 0.05$, **$p < 0.01$. ***c***, Correlations between the strengths of WM codes and RT for each ROI. Each dot represents each participant.

WM representational space is reorganized over time

The RSA analyses revealed multiplexing of representational codes supporting WM in both the IPS and VC. To more directly visualize these representations, we turned to multidimensional scaling (MDS) which helps to elucidate representational geometry. For each delay period, region, and time point, we submitted the similarity structure of the 10 spatial locations to MDS and plotted each location in the space formed by the first three dimensions (see Materials and Methods). We performed this analysis in two ways. First, we trained and tested on a TR-by-TR basis as we did with the cross-hemifield decoding analysis. This allows visualization of the dominant geometry over time (dominant geometry). Second, we trained on the end of the post-cue delay (12 and 14 s post-stimulus onset) as we did with the temporal generalization and representational similarity analyses. This allows honing in on mnemonic codes (mnemonic geometry).

Each analysis revealed a clear geometry during each delay period and transformation of the representations supporting WM over time. Starting with the dominant geometry, during the "pre-cue" period, representations were separated by hemifield along the first dimension in both the IPS and VC (Fig. 6*b*, Fig. S5*b*). For both areas, a clear circular geometry was present across the second and third dimensions resembling the structure of the visually presented locations (Fig. 6*b*, Fig. S5*c*). Across hemifields these circular structures were vertically aligned but mirror-reversed consistent with distance in retinotopic space (e.g., position 2 in the left hemifield is close to position 1 in the right hemifield; Fig. 6*a*). Hence, retinotopic space was well recapitulated across the three dimensions of MDS in both the IPS and VC. Similar results were obtained in the VC for the mnemonic geometry (Fig. 6*c*). In the IPS, the mnemonic geometry was also split by hemifield. However, in this case, the sequence positions across the hemifields were aligned along the second and third dimensions. Thus, the mnemonic geometry revealed evidence of abstraction. These data indicate that retinotopic and abstract sequence codes were multiplexed in the IPS, while the VC represented retinotopic codes.

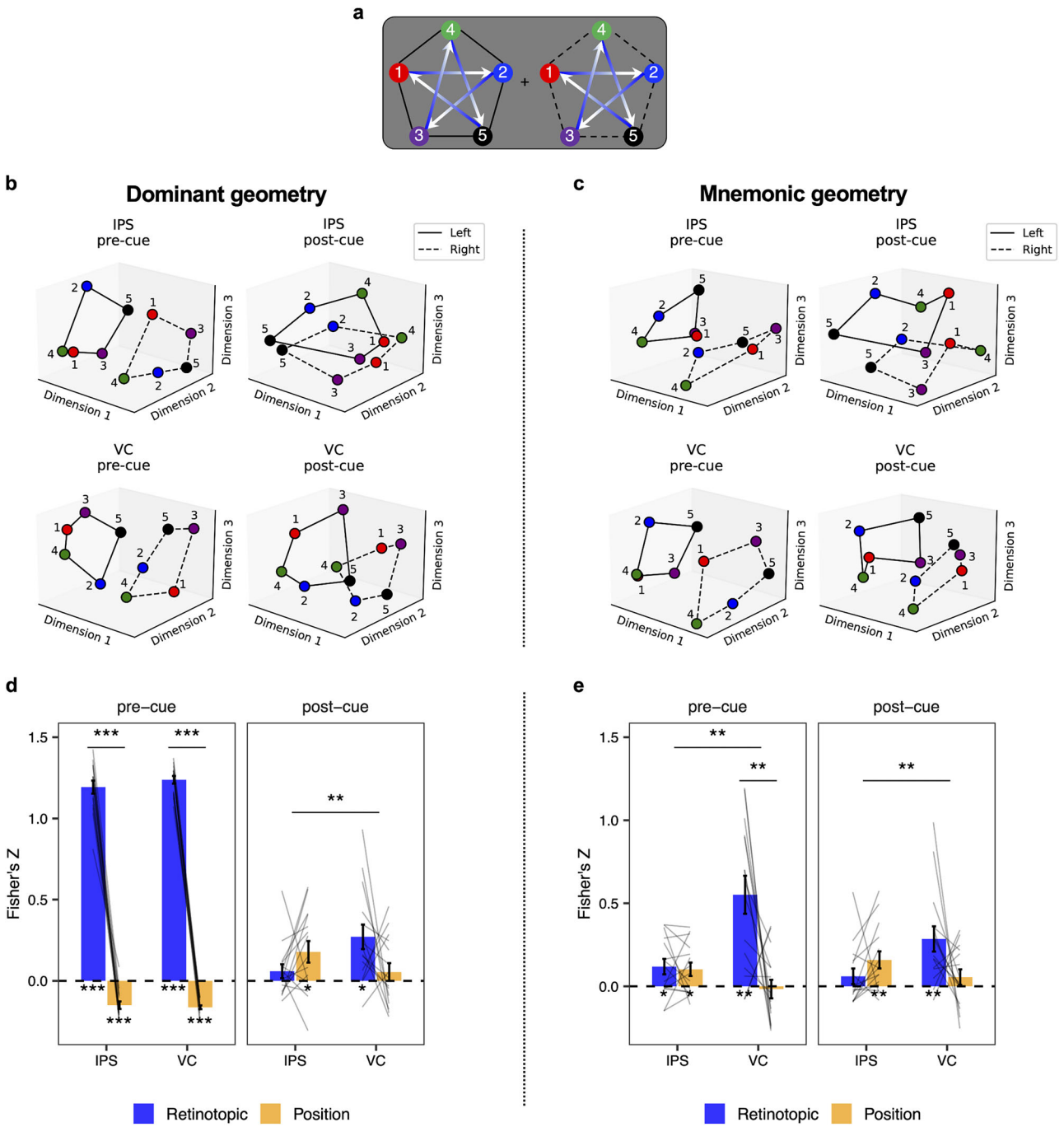

Figure 6. Representational geometry of WM. ***a***, Schematic illustration of the spatial locations. ***b***, Each of the 10 spatial locations is plotted by the first three dimensions of the group-level dominant MDS geometry. Spatial locations are separately color coded by sequence position. Spatial locations in the left and right visual hemifields are connected by solid and dotted black lines, respectively. ***c***, Each of the 10 spatial locations is plotted by the first three dimensions of the group-level mnemonic MDS geometry. Spatial locations are separately color coded by sequence position. Spatial locations in the left and right visual hemifields are connected by solid and dotted black lines, respectively. ***d***, The result of the correlation between Euclidean distance among locations calculated in retinotopic space (blue) and position space (orange) and the dominant MDS geometry space. Note that the correlation analysis was performed at the individual participant level. Each line on the bar graph represents each participant. $*p < 0.05$, $**p < 0.01$, $***p = 0.001$. Error bars represent ±1 standard error of mean. ***e***, The result of the correlation between Euclidean distance among locations calculated in retinotopic space (blue) and position space (orange) and the mnemonic MDS geometry space. Note that the correlation analysis was performed at the individual participant level. Each line on the bar graph represents each participant. $*p < 0.05$, $**p < 0.01$, $***p = 0.001$. Error bars represent ±1 standard error of mean.

In the "post-cue" period, the dominant geometry and mnemonic geometry were similar to one another in the IPS and VC, respectively, but differed across regions. In the IPS, hemifield discrimination was reduced and relegated to the third dimension (Fig. 6*b*,*c*). A circular geometry resembling the star-sequence was observed along the first and second dimensions (Fig. S5*b*,*e*). These circular geometries were aligned by position across hemifields. In VC, hemifield discrimination remained prominent along the first dimension. Alignment by sequence position was also observed in VC, albeit across the second and third dimensions (Fig. S5*c*,*f*). That is, the "post-cue" geometry in the VC resembled the "pre-cue" mnemonic geometry of the IPS. Hence, representational transformations were observed in both the IPS and VC transitioning away from a concrete, retinotopic

codes toward abstract, position codes. However, the areas differed in their principal coding axis. The IPS more prominently coded for sequence position while the VC more prominently coded for hemifield.

To quantitatively evaluate the representational dynamics in the multidimensional space, we examined the extent to which Euclidean distance among representations in each of the dominant and mnemonic geometries resembled retinotopic distance and abstract position distance. Retinotopic distance was calculated as the distance in visual angle among spatial locations. Position distance was calculated similarly but assumed that positions across hemifields were identical (Fig. S5*g*,*h*). For each subject, we correlated the matrix of Euclidean distances in each MDS geometry with the matrix of visual angle distances in retinotopic and position space, respectively, separately for the pre- and post-cue delays. Correlation values were *z*-transformed and submitted to a period ("pre-cue" vs "post-cue") by region (IPS vs VC) by space (retinotopic vs position) repeated-measures ANOVA (Fig. 6*d*,*e*).

For the dominant geometry, we found a significant three-way interaction ($F_{(1,14)} = 5.44$, $p = 0.035$; see Table 1 for complete stats). Specifically, in the "pre-cue" period, the representational geometry closely resembled retinotopic space much more so than position space in both the IPS and VC (region × space repeated-measures ANOVA in the "pre-cue" period; main effect of space; $F_{(1,14)} = 2{,}181.08$, $p = 0.001$). In contrast, in the "post-cue" period, the IPS representational geometry was more similar to the sequence position space than the retinotopic space, whereas the reverse was true in the VC representational geometry (region × space repeated-measures ANOVA in the "post-cue" period; region × space interaction: $F_{(1,14)} = 12.72$, $p = 0.004$). For the mnemonic geometry, a three-way interaction was not significant ($F_{(1,14)} > 1.63$, $p = 0.222$; see Table 2 for complete stats). Instead, a significant region × space interaction was observed ($F_{(1,14)} = 14.05$, $p = 0.003$) driven by more prominent retinotopic than abstract position coding in the VC in both the "pre-cue" and "post-cue" delays with the opposite true of the IPS. Nearly identical results were observed when repeating this analysis using the full MDS space rather than the first three dimensions.

Taken together, these results suggest that representational geometries in the IPS and VC were organized in a different manner. Specifically, concrete, retinotopic, and abstract, sequence position codes were multiplexed in the "pre-cue" delay in the IPS. Over time, retinotopic coding gave way to abstract sequence position codes. In contrast, VC representational geometry was dominated by a concrete, retinotopic code across delays.

Discussion

Although WM guides future cognition (Nobre and Stokes, 2019), the mechanisms supporting the transformation of the past into abstract codes that prepare for the future have been elusive. Here, we found evidence for concrete, retrospective codes in the VC and the IPS when human participants maintained past sensory information. Over time concrete, retrospective codes disappeared concomitant with the appearance of prospective codes. This transition was marked by the emergence of abstract sequence position codes in the IPS. Moreover, the strength of abstract prospective coding in the IPS was related to efficient behavioral performance consistent with a signal that prepares for future cognition. Lastly, dimensionality reduction (MDS) revealed that concrete, sensory, and abstract sequence position codes were simultaneously present in the IPS early in the delay. Over time, sensory codes dissipated and abstract sequence position codes dominated. In contrast, representations in the VC remained more sensory-like both early and late. Taken together, these results detail how WM transforms to support future cognition with dissociable roles of VC more strongly representing concrete, sensory-like codes and the IPS more strongly representing the abstract future.

Substantial work has revealed that concrete retrospective sensory signals can be decoded in the IPS and VC during WM delay periods (Harrison and Tong, 2009; Serences et al., 2009; Ester et al., 2015; Bettencourt and Xu, 2016; Sprague et al., 2016; Rademaker et al., 2019). These findings have led to the conclusion that both regions serve as critical sites for the storage of visual WM. However, a central function of WM is the transformation of past information into future-relevant information. Studies have provided evidence for prospective coding of anticipated actions (van Ede et al., 2019; Boettcher et al., 2021), spatial locations (Gunseli et al., 2024; Liu et al., 2024), and visual objects (Lewis-Peacock and Postle, 2008; Lewis-Peacock et al., 2012). Building on these findings, our data show that the representation of past spatial locations in the IPS and VC transform into anticipated spatial positions when preparing for a sequential probe. Moreover, representational geometry analyses revealed that representational codes become abstracted away from sensation such that locations that are retinotopically distant nevertheless align in representation space when they share meaningful features (Courellis et al., 2024). This result implies that the IPS and VC store not only the concrete past but also the anticipated future, with the future stored in a more abstract format than the past. These data are consistent with suggestions that abstraction facilitates planning for the future (Ho et al., 2019).

Table 1. Repeated-measures ANOVA results associated with Figure 6*d*

RM ANOVA	Factors	*F*	*p*
3-way	Space	180.750	0.001
	Period	116.943	0.001
	Region	2.233	0.151
	Space × period	297.681	0.001
	Region × space	14.571	0.003
	Period × region	0.610	0.465
	Space × period × region	5.439	0.035
2-way ("pre-cue" period)	Space	2,181.076	0.001
	Region	0.720	0.429
	Region × space	0.943	0.335
2-way ("post-cue" period)	Space	0.312	0.579
	Region	1.781	0.218
	Region × space	12.716	0.004

Fisher transformed correlation value was submitted to each RM ANOVA.

Table 2. Repeated-measures ANOVA results associated with Figure 6*e*

RM ANOVA	Factors	*F*	*p*
3-way	Space	7.902	0.014
	Period	3.318	0.083
	Region	21.762	0.001
	Space × period	5.783	0.029
	Region × space	14.045	0.003
	Period × region	2.864	0.104
	Space × period × region	1.631	0.222
2-way ("pre-cue" period)	Space	14.498	0.001
	Region	10.659	0.004
	Region × space	9.113	0.007
2-way ("post-cue" period)	Space	0.651	0.433
	Region	9.431	0.013
	Region × space	11.493	0.003

Fisher transformed correlation value was submitted to each RM ANOVA.

Our findings align with evidence for the dissociable contribution of the IPS and VC to visual WM. For example, the presence of a distractor during a WM delay disrupts or biases WM representations in the VC, whereas WM representations in the IPS are robust against distractors (Bettencourt and Xu, 2016; Lorenc et al., 2018; Rademaker et al., 2019). This implies that the IPS may store not only concrete, sensory-like WM codes but also non-stimulus-driven WM representations that are transformed away from the sensory signals (Rademaker et al., 2019). Consistent with this, our data show both concrete sensory and abstract position signals in the IPS with concrete representations transitioning into abstract representations over time. In contrast, transformations and transitions in the VC were weaker. The hints of such signaling in the VC may be due to top-down signals from the IPS. Such an idea is consistent with recent work showing that during WM delays, the IPS shapes the contents of VC through feedback (Xu, 2023), which could potentially be examined in future work by distinguishing representations across layers of VC (van Kerkoerle et al., 2017; Lawrence et al., 2018). Moreover, the strength of abstract prospective codes in the IPS were related to improved behavior. Collectively, these data indicate dissociable roles of the VC and IPS with the former involved in concrete, sensory representation and the latter important when abstract, prospective codes facilitate performance (Brincat et al., 2018). These data are broadly consistent with cortical progressions from sensory to more abstract coding (Mesulam, 1998; Brincat et al., 2018).

Recent work has shown that VC representations supporting WM can generalize across gratings and motion directions into an abstract line-like format (Kwak and Curtis, 2022) and can show invariance to aperture biases (Duan and Curtis, 2024). In those works, generalization was examined within the same spatial receptive field. Here, we examined generalization across spatial receptive fields (i.e., across visual hemifields). Hence, that abstract coding was weak or absent in the VC in our data does not undermine the presence of other forms of abstract coding in the VC. Rather, there may well be different levels of abstraction which transition across the visual hierarchy. Since we did not perform retinotopic mapping to carefully tease apart different levels of the visual hierarchy, here examination of how abstract coding in the present task varies along the levels of the visual hierarchy is a question for future work.

Some work has indicated that WM for features (i.e., orientation) is represented in a spatially global manner in VC (Ester et al., 2009). Even in perception, neurons and voxels tuned to particular features show elevated activity for preferred features that are presented outside of their receptive fields (Treue and Martinez Trujillo, 1999; Serences and Boynton, 2007). Spatially generalized coding of features may facilitate the detection of behaviorally relevant features when their location is uncertain such as in visual search. However, it is unclear whether the spatially global spread of feature coding observed in those cases and the generalization of spatial position observed here reflect similar mechanisms. In either case, similar to what we observe here, Ester et al. (2009) did not observe cross-hemifield generalization in VC despite the ability to decode orientations held in WM from ipsilateral VC. This suggests that VC retains some element of spatial specificity in its coding.

Abstraction in WM is thought to transform its representational structure—reflecting past content—into a future-oriented format to guide the upcoming task (Myers et al., 2017; Wang et al., 2019; Xie et al., 2022; van Ede and Nobre, 2023). Panichello and Buschman (2021) contrasted selection from WM with selection from perception (i.e., attention) in monkeys. They found that selection in both forms generalized in the prefrontal cortex (PFC), providing evidence for an abstract mechanism of control. Moreover, PFC representations of WM items transformed from a pre-cue subspace wherein WM representations for different colors were multiplexed with location, to a post-cue subspace wherein representations for different colors aligned regardless of location. The same transformation in representational geometry was also observed in a recurrent neural network trained to carry out an equivalent cued-recall paradigm (Piwek et al., 2023; see also Wan et al., 2024). Here, we observed a similar transformational alignment (i.e., from retinotopic space to sequence position space), particularly in the IPS. Observing these signals in the IPS here may be due to the fact that spatial information remained relevant for the task and that the IPS and other dorsal stream areas are important for the representation of space (Mishkin et al., 1983). These findings align with the proposition that abstraction in WM is reflected in the transformation of representational structure into a future-oriented format.

Consistent with past work, we show that sensory and mnemonic information are multiplexed in the IPS (Rademaker et al., 2019). Importantly, training classifiers during periods far removed from perception enabled our analyses to focus on mnemonic representations, thus ruling out that the transformations observed here simply reflect a shift from perception to memory. However, training classifiers on the pre-cue delay also demonstrated a transition from retrospective to prospective (Fig. S4*a*) and concrete to abstract (Fig. S4*c*), albeit with greater emphasis on retrospective and concrete codes. These results indicate that while the patterns observed here are robust across training periods, different analysis approaches can emphasize either sensory-like or abstract codes within the multiplexed representations (Iamshchinina et al., 2021).

One potential approach for examining the contents of WM in a more time-resolved manner would be to analyze eye movements. Recent studies have shown that microsaccades and/or spatial biases in gaze dynamically track the spatial locus of working memory (van Ede et al., 2019; van Ede et al., 2021; Liu et al., 2022; Liu et al., 2024). This is consistent with the close link among eye movements, attention, and WM (Ikkai and Curtis, 2011; Jerde et al., 2012; Jerde and Curtis, 2013). Hence, it is likely that subtle changes in eye position may track the contents of WM in the present study. However, how eye position relates to the maintenance of abstract codes that are not tied to any one position in space remains an open question. This would be a fruitful topic of future study.

In sum, a combination of multivariate decoding, RSA, and MDS revealed that both IPS and VC initially maintained concrete past locations. Over time, these representations became progressively more abstract and prospective especially in the IPS. These results suggest that WM guides future cognition by reformatting sensory signals of the past into more abstract codes to guide prospective expectations.

References

Albers AM, Kok P, Toni I, Dijkerman HC, de Lange FP (2013) Shared representations for working memory and mental imagery in early visual cortex. Curr Biol 23:1427–1431.

Andersson JL, Hutton C, Ashburner J, Turner R, Friston K (2001) Modeling geometric deformations in EPI time series. Neuroimage 13:903–919.

Ashburner J, Friston K (1997) Multimodal image coregistration and partitioning–a unified framework. Neuroimage 6:209–217.

Baddeley A (1992) Working memory. Science 255:556–559.

Badre D (2024) Cognitive control. Annu Rev Psychol 76:167–195.
Badre D, D'Esposito M (2007) Functional magnetic resonance imaging evidence for a hierarchical organization of the prefrontal cortex. J Cogn Neurosci 19:2082–2099.
Badre D, Kayser AS, D'Esposito M (2010) Frontal cortex and the discovery of abstract action rules. Neuron 66:315–326.
Badre D, Bhandari A, Keglovits H, Kikumoto A (2021) The dimensionality of neural representations for control. Curr Opin Behav Sci 38:20–28.
Benjamini Y, Hochberg Y (1995) Controlling the false discovery rate - a practical and powerful approach to multiple testing. J R Stat Soc B 57:289–300.
Bernardi S, Benna MK, Rigotti M, Munuera J, Fusi S, Salzman CD (2020) The geometry of abstraction in the hippocampus and prefrontal cortex. Cell 183:954–967.e21.
Bettencourt KC, Xu Y (2016) Decoding the content of visual short-term memory under distraction in occipital and parietal areas. Nat Neurosci 19:150–157.
Boettcher SEP, Gresch D, Nobre AC, van Ede F (2021) Output planning at the input stage in visual working memory. Sci Adv 7:eabe8212.
Brincat SL, Siegel M, von Nicolai C, Miller EK (2018) Gradual progression from sensory to task-related processing in cerebral cortex. Proc Natl Acad Sci U S A 115:E7202–E7211.
Christophel TB, Hebart MN, Haynes JD (2012) Decoding the contents of visual short-term memory from human visual and parietal cortex. J Neurosci 32:12983–12989.
Christophel TB, Cichy RM, Hebart MN, Haynes JD (2015) Parietal and early visual cortices encode working memory content across mental transformations. Neuroimage 106:198–206.
Chunharas C, Wolff M, Hettwer M, Rademaker R (2025) A gradual transition toward categorical representations along the visual hierarchy during working memory, but not perception. Elife 14:RP103347.
Collins AG, Frank MJ (2013) Cognitive control over learning: creating, clustering, and generalizing task-set structure. Psychol Rev 120:190–229.
Combrisson E, Jerbi K (2015) Exceeding chance level by chance: the caveat of theoretical chance levels in brain signal classification and statistical assessment of decoding accuracy. J Neurosci Methods 250:126–136.
Courellis HS, Minxha J, Cardenas AR, Kimmel DL, Reed CM, Valiante TA, Salzman CD, Mamelak AN, Fusi S, Rutishauser U (2024) Abstract representations emerge in human hippocampal neurons during inference. Nature 632:841–849.
Curtis CE, D'Esposito M (2003) Persistent activity in the prefrontal cortex during working memory. Trends Cogn Sci 7:415–423.
D'Esposito M, Postle BR (2015) The cognitive neuroscience of working memory. Annu Rev Psychol 66:115–142.
Duan ZY, Curtis CE (2024) Visual working memories are abstractions of percepts. Elife 13:RP94191.
Ester EF, Serences JT, Awh E (2009) Spatially global representations in human primary visual cortex during working memory maintenance. J Neurosci 29:15258–15265.
Ester EF, Sprague TC, Serences JT (2015) Parietal and frontal cortex encode stimulus-specific mnemonic representations during visual working memory. Neuron 87:893–905.
Fuster JM (1990) Prefrontal cortex and the bridging of temporal gaps in the perception-action cycle. Ann N Y Acad Sci 608:318–329. discussion 330-316.
Fuster JM (2001) The prefrontal cortex–an update: time is of the essence. Neuron 30:319–333.
Gunseli E, Foster JJ, Sutterer DW, Todorova L, Vogel EK, Awh E (2024) Encoded and updated spatial working memories share a common representational format in alpha activity. iScience 27:108963.
Harrison SA, Tong F (2009) Decoding reveals the contents of visual working memory in early visual areas. Nature 458:632–635.
Henderson MM, Rademaker RL, Serences JT (2022) Flexible utilization of spatial- and motor-based codes for the storage of visuo-spatial information. Elife 11:e75688.
Ho MK, Abel D, Griffiths TL, Littman ML (2019) The value of abstraction. Curr Opin Behav Sci 29:111–116.
Iamshchinina P, Christophel TB, Gayet S, Rademaker RL (2021) Essential considerations for exploring visual working memory storage in the human brain. Vis Cogn 29:425–436.
Ikkai A, Curtis CE (2011) Common neural mechanisms supporting spatial working memory, attention and motor intention. Neuropsychologia 49:1428–1434.
Jerde TA, Curtis CE (2013) Maps of space in human frontoparietal cortex. J Physiol Paris 107:510–516.
Jerde TA, Merriam EP, Riggall AC, Hedges JH, Curtis CE (2012) Prioritized maps of space in human frontoparietal cortex. J Neurosci 32:17382–17390.
Jones HM, Diaz GK, Ngiam WXQ, Awh E (2024) Electroencephalogram decoding reveals distinct processes for directing spatial attention and encoding into working memory. Psychol Sci 35:1108–1138.
King JR, Dehaene S (2014) Characterizing the dynamics of mental representations: the temporal generalization method. Trends Cogn Sci 18:203–210.
Kriegeskorte N, Mur M, Bandettini P (2008) Representational similarity analysis - connecting the branches of systems neuroscience. Front Syst Neurosci 2:4.
Kumar M, Ellis CT, Lu Q, Zhang H, Capota M, Willke TL, Ramadge PJ, Turk-Browne NB, Norman KA (2020) Brain IAK tutorials: user-friendly learning materials for advanced fMRI analysis. PLoS Comput Biol 16:e1007549.
Kwak Y, Curtis CE (2022) Unveiling the abstract format of mnemonic representations. Neuron 110:1822–1828.e5.
Lapate RC, Ballard IC, Heckner MK, D'Esposito M (2022) Emotional context sculpts action goal representations in the lateral frontal pole. J Neurosci 42:1529–1541.
LaRocque JJ, Riggall AC, Emrich SM, Postle BR (2017) Within-category decoding of information in different attentional states in short-term memory. Cereb Cortex 27:4881–4890.
Lawrence SJD, van Mourik T, Kok P, Koopmans PJ, Norris DG, de Lange FP (2018) Laminar organization of working memory signals in human visual cortex. Curr Biol 28:3435–3440.e4.
Lewis-Peacock JA, Postle BR (2008) Temporary activation of long-term memory supports working memory. J Neurosci 28:8765–8771.
Lewis-Peacock JA, Drysdale AT, Oberauer K, Postle BR (2012) Neural evidence for a distinction between short-term memory and the focus of attention. J Cogn Neurosci 24:61–79.
Li HH, Curtis CE (2023) Neural population dynamics of human working memory. Curr Biol 33:3775–3784.e4.
Liu B, Nobre AC, van Ede F (2022) Functional but not obligatory link between microsaccades and neural modulation by covert spatial attention. Nat Commun 13:3503.
Liu BW, Alexopoulou ZS, van Ede F (2024) Jointly looking to the past and the future in visual working memory. Elife 12:RP90874.
Lorenc ES, Sreenivasan KK, Nee DE, Vandenbroucke ARE, D'Esposito M (2018) Flexible coding of visual working memory representations during distraction. J Neurosci 38:5267–5276.
Lorenc ES, Vandenbroucke ARE, Nee DE, de Lange FP, D'Esposito M (2020) Dissociable neural mechanisms underlie currently-relevant, future-relevant, and discarded working memory representations. Sci Rep 10:11195.
Lund TE, Nørgaard MD, Rostrup E, Rowe JB, Paulson OB (2005) Motion or activity: their role in intra-and inter-subject variation in fMRI. Neuroimage 26:960–964.
Mesulam MM (1998) From sensation to cognition. Brain 121:1013–1052.
Mishkin M, Ungerleider LG, Macko KA (1983) Object vision and spatial vision: two cortical pathways. Trends Neurosci 6:414–417.
Murray JD, Bernacchia A, Roy NA, Constantinidis C, Romo R, Wang XJ (2017) Stable population coding for working memory coexists with heterogeneous neural dynamics in prefrontal cortex. Proc Natl Acad Sci U S A 114:394–399.
Myers NE, Rohenkohl G, Wyart V, Woolrich MW, Nobre AC, Stokes MG (2015) Testing sensory evidence against mnemonic templates. Elife 4:e09000.
Myers NE, Stokes MG, Nobre AC (2017) Prioritizing information during working memory: beyond sustained internal attention. Trends Cogn Sci 21:449–461.
Nasrawi R, van Ede F (2022) Planning the potential future during multi-item visual working memory. J Cogn Neurosci 34:1534–1546.
Nee DE, D'Esposito M (2016) The hierarchical organization of the lateral prefrontal cortex. Elife 5:e12112.
Nee DE, D'Esposito M (2018) The representational basis of working memory. Curr Top Behav Neurosci 37:213–230.
Nobre AC, Stokes MG (2019) Premembering experience: a hierarchy of timescales for proactive attention. Neuron 104:132–146.
Panichello MF, Buschman TJ (2021) Shared mechanisms underlie the control of working memory and attention. Nature 592:601–605.
Pasternak T, Greenlee MW (2005) Working memory in primate sensory systems. Nat Rev Neurosci 6:97–107.

Pedregosa F (2011) Scikit-learn: machine learning in Python. J Mach Learn Res 12:2825–2830.
Piwek EP, Stokes MG, Summerfield C (2023) A recurrent neural network model of prefrontal brain activity during a working memory task. PLoS Comput Biol 19:e1011555.
Rademaker RL, Chunharas C, Serences JT (2019) Coexisting representations of sensory and mnemonic information in human visual cortex. Nat Neurosci 22:1336–1344.
Rainer G, Rao SC, Miller EK (1999) Prospective coding for objects in primate prefrontal cortex. J Neurosci 19:5493–5505.
Riggall AC, Postle BR (2012) The relationship between working memory storage and elevated activity as measured with functional magnetic resonance imaging. J Neurosci 32:12990–12998.
Scimeca JM, Kiyonaga A, D'Esposito M (2018) Reaffirming the sensory recruitment account of working memory. Trends Cogn Sci 22:190–192.
Serences JT (2016) Neural mechanisms of information storage in visual short-term memory. Vision Res 128:53–67.
Serences JT, Boynton GM (2007) Feature-based attentional modulations in the absence of direct visual stimulation. Neuron 55:301–312.
Serences JT, Ester EF, Vogel EK, Awh E (2009) Stimulus-specific delay activity in human primary visual cortex. Psychol Sci 20:207–214.
Shushruth S, Zylberberg A, Shadlen MN (2022) Sequential sampling from memory underlies action selection during abstract decision-making. Curr Biol 32:1949.
Sprague TC, Serences JT (2013) Attention modulates spatial priority maps in the human occipital, parietal and frontal cortices. Nat Neurosci 16:1879–1887.
Sprague TC, Ester EF, Serences JT (2014) Reconstructions of information in visual spatial working memory degrade with memory load. Curr Biol 24:2174–2180.
Sprague TC, Ester EF, Serences JT (2016) Restoring latent visual working memory representations in human cortex. Neuron 91:694–707.
Sreenivasan KK, D'Esposito M (2019) The what, where and how of delay activity. Nat Rev Neurosci 20:466–481.
Treue S, Martinez Trujillo JC (1999) Feature-based attention influences motion processing gain in macaque visual cortex. Nature 399:575–579.
van Ede F, Deden J, Nobre AC (2021) Looking ahead in working memory to guide sequential behaviour. Curr Biol 31:R779–R780.
van Ede F, Nobre AC (2023) Turning attention inside out: how working memory serves behavior. Annu Rev Psychol 74:137–165.
van Ede F, Chekroud SR, Stokes MG, Nobre AC (2019) Concurrent visual and motor selection during visual working memory guided action. Nat Neurosci 22:477–483.
van Kerkoerle T, Self MW, Roelfsema PR (2017) Layer-specificity in the effects of attention and working memory on activity in primary visual cortex. Nat Commun 8:13804.
Wan Q, Ardalan A, Fulvio JM, Postle BR (2024) Representing context and priority in working memory. J Cogn Neurosci 36:1374–1394.
Wang LP, Amalric M, Fang W, Jiang XJ, Pallier C, Figueira S, Sigman M, Dehaene S (2019) Representation of spatial sequences using nested rules in human prefrontal cortex. Neuroimage 186:245–255.
Wang L, Mruczek REB, Arcaro MJ, Kastner S (2015) Probabilistic maps of visual topography in human cortex. Cereb Cortex 25:3911–3931.
Xie Y, et al. (2022) Geometry of sequence working memory in macaque prefrontal cortex. Science 375:632.
Xu YD (2023) Parietal-driven visual working memory representation in occipito-temporal cortex. Curr Biol 33:4516. +.
Yu Q, Teng C, Postle BR (2020) Different states of priority recruit different neural representations in visual working memory. PLoS Biol 18:e3000769.